Applied Catalysis B: Environment and Energy 375 (2025) 125443

Contents lists available at ScienceDirect

Applied Catalysis B: Environment and Energy

journal homepage: www.elsevier.com/locate/apcatb

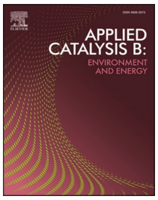

Effective electrocatalytic xylose oxidation coupling hydrogen production on hierarchical microcolumn $NiMoO_4$ array

Bin Liu [a], Huiming Wen [a], Bo Da [b], Xiaoying Liang [a], Ke Li [a], Zhenhao Xu [a], Xiaodie Zhang [a], Yutong Zhang [a], Yuchen Wang [a], Hao Li [b,c,*], Kai Yan [a,**]

[a] Guangdong Provincial Key Laboratory of Environmental Pollution Control and Remediation Technology, School of Environmental Science and Engineering, Sun Yat-sen University, Guangzhou 510275, China
[b] Center for Basic Research on Materials, National Institute for Materials Science, Tsukuba, Ibaraki 305-0047, Japan
[c] Advanced Institute for Materials Research (WPI-AIMR), Tohoku University, Sendai 980-8577, Japan

ARTICLE INFO

Keywords:
Electrocatalytic xylose oxidation
Hydrogen evolution reaction
Coupling
$NiMoO_4$ microcolumn
Hydrogen production

ABSTRACT

The simultaneous realization of biomass conversion and clean energy hydrogen (H_2) production remains a desirable but challenging objective. Herein, we present a strategy that simultaneously enables anodic electrocatalytic xylose oxidation (EXO) coupling with the cathodic hydrogen evolution reaction (HER). In the EXO process, the hierarchical microcolumn $NiMoO_4$ array exhibits excellent performance, achieving 200 and 231 mV reduction of overpotential compared to the oxygen evolution reaction at 10 and 50 mA cm^{-2}, respectively, and an overpotential of 130 mV lower than that of Ni foam at 50 mA cm^{-2}. The mechanism studies reveal that the OH* are effective active species to facilitate the EXO process. For HER, the P-doped $NiMoO_4$ (P-$NiMoO_4$) electrode exhibits remarkable HER performance, achieving 64 and 197 mV overpotential at 10 and 50 mA•cm^{-2}, respectively. These are far superior to most of the previous studies. The P-$NiMoO_4$ electrode maintains high durability over 110 h across various current densities. The incorporation of P modifies the electronic environment of $NiMoO_4$, enhancing the adsorption of H* , and thereby improving HER activity. In the assembled system, the paired reactions have low voltages of 0.81 and 1.53 V at 10 and 50 mA cm^{-2}, respectively, a high Faradaic efficiency of 80 %, and decent durability over 100 h. This work offers a guideline for the sustainable synthesis of value-added chemicals and clean H_2 via paired electrocatalytic biomass refining.

1. Introduction

Exploring clean and sustainable energy alternatives to fossil resources has been recognized as an effective strategy for mitigating the energy crisis [1–3]. Hydrogen (H_2) has received much attention as a clean and renewable energy source with sustainable and carbon-neutral potential recently [4,5]. Electrocatalytic water splitting (EWS) technology powered by renewable green electricity is an economical and eco-friendly approach for H_2 production [6–9]. However, the inherent thermodynamic energy barriers (>1.23 V *vs.* reversible hydrogen electrode, RHE) for the anodic oxygen evolution reaction (OER) severely hinder the practical application. Moreover, the sluggish kinetics of O═O bond formation in OER leads to the need for high overpotentials to match the rate of the hydrogen evolution reaction (HER) [10–12]. Thus, from the point of view of reducing energy consumption and improving economic efficiency, finding a more favorable alternative for OER at the anode is essential.

Over the last decades, an attractive system has been proposed with small molecules (*e.g.*, hydrazine [13–15]. alcohols [16,17], urea [18–20], biomass platform molecules [21]), which are used as sacrificial agents for electrochemical oxidation to replace the anodic OER, and which reduces the anodic reaction potential. Among these systems, the biomass electrooxidation coupling HER system, which can convert biomass into valuable chemicals while efficiently producing H_2 from water splitting, represents the most eco-friendly and promising technology [21]. Monomers from lignocellulosic biomass, such as xylose, arabinose, fructose, and glucose, can be oxidatively converted to a variety of value-added chemicals [22]. Recently, Wu and co-workers reported the oxidative conversion of glucose to high value-added gluconic acid using a high entropy hydroxide FeCoNiCu-LDHs catalyst, together

---

* Corresponding author at: Center for Basic Research on Materials, National Institute for Materials Science, Tsukuba, Ibaraki 305-0047, Japan.
** Corresponding author.
E-mail addresses: li.hao.b8@tohoku.ac.jp (H. Li), yank9@mail.sysu.edu.cn (K. Yan).

https://doi.org/10.1016/j.apcatb.2025.125443
Received 26 March 2025; Received in revised form 29 April 2025; Accepted 4 May 2025

with a high glucose conversion of ~100 % and glucaric acid yield of > 90 % [23]. Tang and co-workers developed an efficient electrocatalytic glucose-to-formic acid (FA) coupled H_2 production system. Among them, the yield of glucose to FA was as high as 62.5 % [21]. Clearly, the selectivity for the conversion of monosaccharide to FA and the kinetics of the reaction still need to be further improved. Encouraged by the above facts, replacing the OER with a monosaccharide oxidation reaction such as electrocatalytic xylose oxidation (EXO) is a promising strategy to generate more valuable organic acids at the anode while producing energy-saving H_2 at the cathode. This strategy offers a win-win with biomass conversion being coupled with energy production.

Xylose is a five-carbon saccharide with one α-OH and multiple primary alcohols, which is highly reactive and conceivably promises faster kinetic electrooxidation. Nevertheless, the challenge lies in the complex electron transfer process, which renders the anode biomass oxidation reaction rate-limiting and demands highly active catalysts. In addition, the breakage of the carbon chain of xylose leads to a wide variety of products, so it is a big challenge to precisely regulate the selectivity of the products. In recent years, researchers have been focusing on the development of highly efficient non-precious metal electrocatalysts [24–26], among which NiMo-based oxides are considered promising and scalable candidates due to their abundant catalytic sites, high surface area and easy synthesis methods. In particular, the binding of MoO_3 to three-dimensional transition metals plays a crucial role in modifying the hydrolytic dissociation and H_2 adsorption capacity [27]. The in situ generation of metal hydroxides/oxyhydroxides could modulate the adsorption energy of the substrate [28], thus reducing the reaction energy barrier to promote EXO. Additionally, heteroatom doping can adjust the electronic structure of the host material and rearrange the valence electrons, to optimize the adsorption energy of the H intermediate, effectively improving the HER performance of polymetallic compounds without changing chemical composition [29].

Herein, we have successfully constructed the robust EXO coupling H_2 production system using the electrodes which self-grown hierarchical microcolumn $NiMoO_4$ ($NiMoO_4$/NF) and P-$NiMoO_4$ on nickel foam (P-$NiMoO_4$/NF), respectively. In EXO, the pre-synthesized hierarchical microcolumn $NiMoO_4$/NF electrode shows exceptional catalytic performance to generate the value-added FA using 0.1 M xylose and the current density of 10 and 50 mA cm^{-2} can be reached with only 1.33 and 1.39 V_{RHE}, respectively. The overpotential is 130 mV lower than that of NF at 50 mA cm^{-2}. In HER, the P-$NiMoO_4$/NF electrode with the introduction of heteroatomic P can efficiently and robustly catalyze HER with a low overpotential of 64 and 197 mV (@10 and 50 mA cm^{-2}), which are far superior to most previous studies. Particularly, the abundant porous structure over hierarchical microcolumn $NiMoO_4$ array endowed the catalysts with abundant active sites and enhanced mass diffusion kinetics. Mechanism studies demonstrated that the OH* and H* , as essential and effective active substances, promoted EXO and HER, respectively. The two-electrode system assembled by $NiMoO_4$/NF and P-$NiMoO_4$/NF electrodes for coupling EXO and HER only requires low cell voltage of 0.81 and 1.53 V to drive the current density of 10 and 50 mA cm^{-2}, respectively, which are 760 and 450 mV lower than that required for traditional overall EWS. High-value product FA and green H_2 can be generated synchronously and stably over 100 h. This work provides a promising strategy to achieve valuable biomass refining coupled-clean H_2 generation.

2. Experimental section

2.1. Chemical and materials

The following analytical-grade reagents were sourced from National Reagent Company for this investigation: nickel foam (NF), hydrochloric acid (HCl), ethanol (C_2H_5OH), acetone (CH_3COCH_3), nickel nitrate hexahydrate ($Ni(NO_3)_2 \cdot 6\ H_2O$), ammonium molybdate tetrahydrate ($(NH_4)_6Mo_7O_{24} \cdot 4\ H_2O$), sodium hypophosphite monohydrate ($NaH_2PO_2 \cdot H_2O$), and potassium hydroxide (KOH). Commercially available RuO_2 and carbon-supported Pt catalyst (Pt/C, 20 wt% metal loading) were procured from Sigma-Aldrich. All chemical solutions were formulated using deionized (DI) water (18.2 MΩ·cm resistivity) without further treatment. Notably, all materials were employed in their as-received condition without undergoing additional purification processes.

2.2. Preparation of $NiMoO_4 \cdot nH_2O$ precursor

Firstly, the $NiMoO_4 \cdot nH_2O$ precursor grown on nickel foam was prepared by hydrothermal method. The commercial NF was subjected to sequential ultrasonication with acetone, ethanol, HCl solution (2.0 M), and deionized water, each for 30 min. A piece of cleaned NF (1.0 *1.0 cm^2) was immersed in the mixture solution (60.0 mL) containing $Ni(NO_3)_2 \cdot 6\ H_2O$ (1.5 mmol) and $(NH_4)_6Mo_7O_{24} \cdot 4\ H_2O$ (1.5 mmol). Subsequently, the autoclave containing the above mixture was heated in an oven at a temperature of 150 °C for 6 h. Following the rinse with deionized water, the $NiMoO_4 \cdot nH_2O$ precursor was obtained for subsequent experiments.

2.3. Preparation of $NiMoO_4$/NF and P-$NiMoO_4$/NF electrode

The obtained $NiMoO_4 \cdot nH_2O$ precursor was treated at 300 °C for 2 h with a heating rate of 2 °C min^{-1} under Ar atmosphere to get the $NiMoO_4$/NF electrode. After adding $NaH_2PO_2 \cdot H_2O$ as the P source at the same annealing temperature, the P-$NiMoO_4$/NF electrode can be obtained. Further specifics and dosage of the chemical reagents employed in this study are compiled within the Supporting Information. The characterization techniques, electrochemical properties measurements and product quantification are described in Supporting Information.

2.4. Physical characterization

The crystalline structures of $NiMoO_4$ and P-$NiMoO_4$ were characterized using X-ray diffraction (XRD, UltimaIV, RIGAKU) with Cu Kα radiation. Measurements were performed at 40 kV accelerating voltage and 40 mA tube current, employing a scanning speed of 2° min^{-1} over the 2θ range of 10–60°. X-ray photoelectron spectroscopy (XPS) was performed using a Thermo Scientific K-Ala spectrometer equipped with monochromatic Al Kα X-ray source (40 eV pass energy) to characterize the valence states of Ni, Mo, O, and P elements. Hydroxyl radical generation was analyzed using an electron paramagnetic resonance (EPR, Burker A300) spectrometer with 5,5-dimethyl-1-pyrroline N-oxide (DMPO) as a spin-trapping agent. To ensure sample integrity, all EPR characterizations were performed under inert argon atmosphere at ambient temperature. The electrolysis was performed in an H-cell at 1.6 V *vs.* RHE, and electrolyte samples were taken at 5 min for spectroscopic analysis. The microstructural characteristics and crystallographic features of the sample were analyzed through transmission electron microscope (TEM) and high-resolution transmission electron microscope (HRTEM) imaging using an FEI Talos F200x system operated at 200 kV acceleration voltage, which enabled detailed examination of lattice arrangements and interfacial structures. The HRTEM point resolution was 0.2 nm. The surface structural morphology of the catalyst was examined through scanning electron microscopy (SEM, Zeiss Sigma 500) operating at 15 kV with a spatial resolution of 0.8 nm. Elemental distribution analysis was conducted via energy-dispersive X-ray (EDX) spectroscopy using the integrated detector of the Zeiss Sigma 500 detector at 15 kV beam energy.

2.5. Electrochemical measurement

The Autolab M204 electrochemical workstation and a standard three-electrode system, comprising a working electrode, Hg|HgO reference electrode and platinum wire counter electrode. The electrolyte consisted of 10.0 mL Ar-saturated alkaline solution containing 1.0 M KOH and 0.1 M xylose. Electrochemical potentials were referenced to the reversible hydrogen electrode (RHE) through the following potential conversion equation: $E_{RHE} = E^{\Theta}(Hg|HgO) + 0.0591 \times pH + 0.098$. The linear sweep voltammetry (LSV) program was conducted with a 5 mV s^{-1} sweep rate across the 0.9–1.7 V_{RHE} potential window. To investigate the kinetic behavior of electrode processes, electrochemical impedance spectroscopy (EIS) measurements were performed under open-circuit conditions in the frequency range from 10^{-1} to 10^{5} Hz. The electrochemical surface area (ECSA) was determined through cyclic voltammetry (CV) measurements performed across scan rates ranging from 10 to 50 mV s^{-1}. The electrochemical durability of the P-$NiMoO_4$/NF electrode was evaluated through chronoamperometry (CA) in a 10.0 mL homogeneous mixture containing 1.0 M KOH and 0.1 M xylose under the stirring rate of 600 rpm.

The turnover frequency (TOF) is determined according to the following formula:

$$TOF = \frac{j \times A}{n \times F \times m}$$

where j represents the current density under varying overpotentials (mA cm^{-2}), while A denotes the geometric surface area of the working electrode (cm^2). The variable n corresponds to the number of electrons participating in the charge transfer process, F signifies the Faraday constant (96,485 C mol^{-1}), and m quantifies the molar amount of electroactive species in the catalytic system (mol).

2.6. Product quantification

To investigate the substrates and reaction products generated in the EXO process, 100 μL aliquots were periodically collected from the homogenized electrolyte mixture using CA. These samples were subsequently adjusted with 0.5 M sulfuric acid and brought to a final volume of 1.0 mL through dilution. To analyze the substrates and products during the EXO process, 100 μL aliquots were periodically collected from the homogenized electrolyte mixture by CA. These samples were subsequently adjusted with 0.5 M H_2SO_4 and brought to a final volume of 1.0 mL through dilution. The qualitative and quantitative assessments were conducted by HPLC (Shimadzu Prominence SIL-20A) incorporating three key components: a SIL-20A autosampler, a Sepax Carbomix H-NP sugar analytical column, and a UV-differential detection unit. For chromatographic separation, the eluent consisted of 2.5 mM H_2SO_4 solution maintained at a steady flow rate of 0.6 mL min^{-1} throughout the analysis. The liquid specimens underwent filtration utilizing a hydrophilic 0.22 mm porous membrane before analytical procedures. An automated sample introduction system transferred the processed solutions to the thermostated column compartment maintained at 55 °C. Detection parameters were optimized with a fixed wavelength setting (220 nm) on the UV differential detector during the analytical runs. The conversion ($Conv_j$) of xylose and the selectivity (S_j) of oxidation products were calculated by the following equations:

$$Conv_j = \left(\frac{C_0 - C_i}{C_0}\right) \times 100\%$$

$$S_j = \frac{C_j}{C_0 - C_i} \times 100\%$$

where C_i and C_0 represents the instant and initial concentrations of xylose, and C_j represents the amount of xylose consumed corresponding to the products produced, respectively. Concentration values were uniformly expressed in mmol L^{-1} units (mM).

The following equation calculated the total Faradaic efficiency (FE) of EXO:

$$FE = \frac{n_{product} \times C_{product} \times V \times F}{Q_{total}} \times 100\%$$

where $n_{product}$ was the number of electron transfers for each product formation; $C_{product}$ was the concentration of the product (mM); V was the volume of the electrolyte; F was Faraday constant (96485 C mol^{-1}); Q_{total} was the total charge (C) passed during the electrochemical reaction.

3. Results and discussion

3.1. Material synthesis and characterizations

Firstly, $NiMoO_4$-nH_2O precursor self-grown on NF was synthesized by hydrothermal method, subsequently, the hierarchical microcolumn $NiMoO_4$ and P-doping $NiMoO_4$ arrays were obtained by high-temperature annealing and phosphating of $NiMoO_4$-nH_2O precursor in Ar_2 atmosphere, respectively (Figure S1). As prepared $NiMoO_4$/NF and P-$NiMoO_4$/NF electrodes were used for the oxidation of xylose monomer at the anode and efficient H_2 production at the cathode, respectively (Fig. 1a), which offered a win-win methodology with biomass-derived monomers upgrading paired with H_2 generation. After the synthesis of these catalysts, various advanced tools were utilized to study their physical properties. The morphology evolution of catalysts was tracked by SEM. It was determined that the $NiMoO_4$ microcolumn array self-grown on NF after hydrothermal treatment (Figure S2). Thereafter, the hierarchical microcolumn $NiMoO_4$ array with a rich porous structure was obtained by annealing (Fig. 1b). This porous hierarchical microcolumn structure greatly increased the specific surface area of the material, which facilitated the exposure of active sites and the mass transfer with substrates and products on the catalyst surface, thus improving the catalytic performance.

Furthermore, the P-$NiMoO_4$ also exhibited microcolumn array morphology with a rough surface (Fig. 1c). Figure S3 showed the electronic photographs of each step in the synthesis of $NiMoO_4$/NF and P-$NiMoO_4$/NF electrodes. The microstructure of $NiMoO_4$ and P-$NiMoO_4$ catalysts was further investigated by TEM, showing microcolumn morphology (Figs. 1d and 1e), consistent with the finding of SEM images. Furthermore, the internal structure was then analyzed by HRTEM (Figs. 1f and 1g). As evidenced by the detected lattice fringe with planar spacing of 0.618 nm in high crystallinity regions of both $NiMoO_4$ and P-$NiMoO_4$ catalysts were 0.618 nm corresponding to the (110) plane of $NiMoO_4$ well, verifying the crystalline phases of $NiMoO_4$ and the phosphating process did not create new phases. In addition, the uniform distribution of Ni, Mo, O and P in the P-$NiMoO_4$ microcolumn was confirmed by high-angle annular dark-field scanning transmission electron microscopy (HAADF-STEM) coupled with EDX spectroscopy images (Figure S4). XRD patterns were then utilized to analyze the crystal structure of the as-prepared $NiMoO_4 \cdot nH_2O$ precursor, $NiMoO_4$ and P-$NiMoO_4$ catalysts. As shown in Fig. 1h and Figure S5, the diffraction peaks in $NiMoO_4 \cdot nH_2O$ and $NiMoO_4$ catalysts correspond to $NiMoO_4 \cdot nH_2O$ (PDF: 13–0128) and $NiMoO_4$ (PDF: 86–0361), respectively, indicating that the water of crystallization was removed after annealing [30]. In particular, the absence of discernible diffraction peaks associated with P-based crystalline structures was noted (Fig. 1h), indicating that the P was doped into $NiMoO_4$ without forming a new phase.

To determine the surface chemical state, XPS tests were executed. The peaks of Ni 2*p*, Mo 3*d*, O 1 *s* and P 2*p* could be identified in the survey spectrum of $NiMoO_4$ (Figure S6a). The distinct peak of P 2*p* at 134.8 eV was only observed in P-$NiMoO_4$ with an atomic content of 9.8 %, confirming the successful incorporation of P atoms (Figure S6b and Table S1). The introduced P concentration was not sufficient to cause obvious lattice distortion or phase transition. This was also the reason why no obvious peak position shift or new peak appearance is

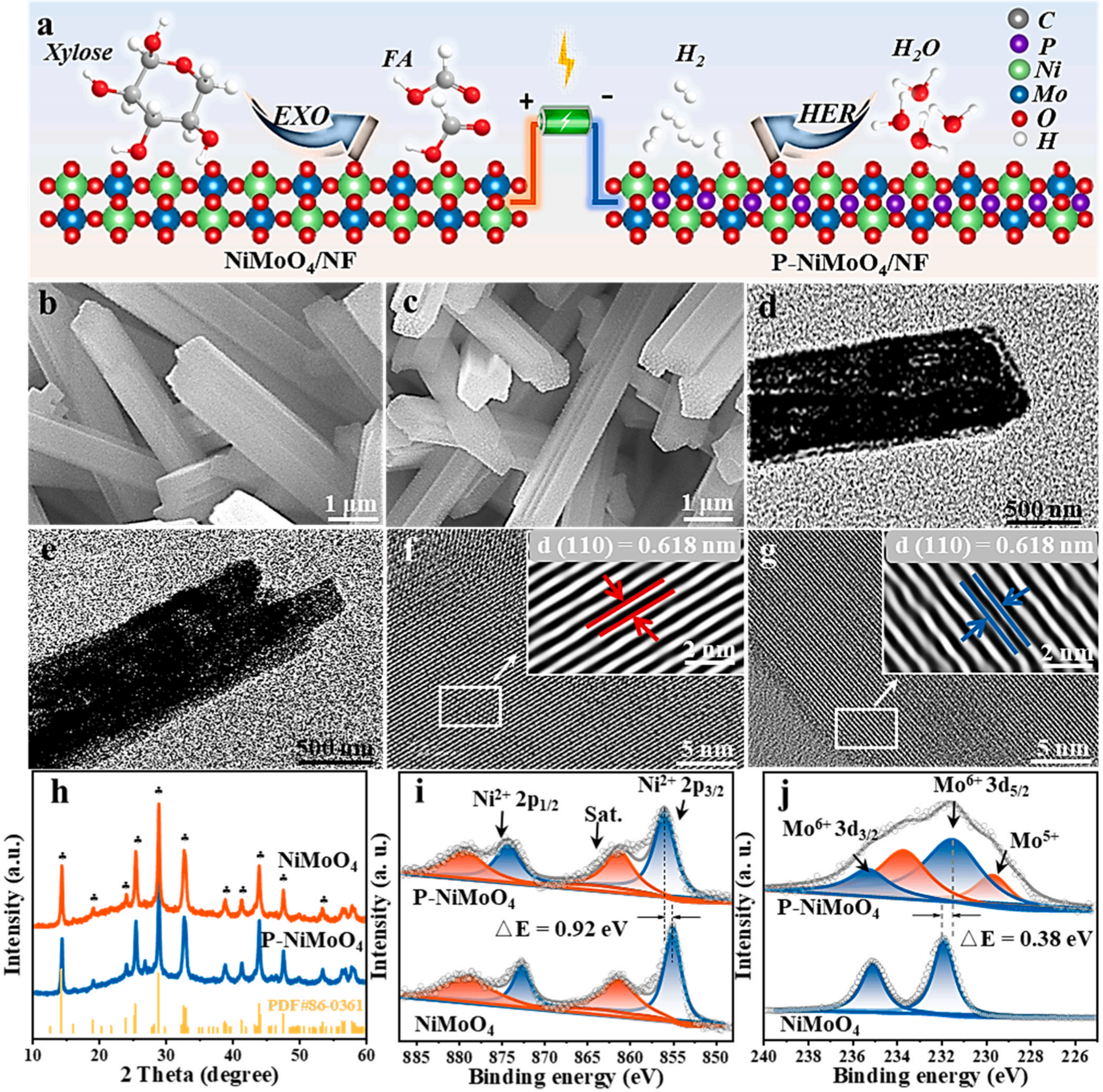

Fig. 1. Morphology characterization of $NiMoO_4$/NF and P-$NiMoO_4$/NF. (a) Schematic illustration of the paired EXO and HER system, SEM images of (b) $NiMoO_4$/NF and (c) P-$NiMoO_4$/NF, TEM of (d) $NiMoO_4$ and (e) P-$NiMoO_4$, HRTEM analysis of (f) $NiMoO_4$ and (g) P-$NiMoO_4$, (h) XRD patterns of $NiMoO_4$ and P-$NiMoO_4$, high solution XPS of (i) Ni 2p and (j) Mo 3d.

observed in XRD. The Ni 2*p* XPS spectra of P-$NiMoO_4$ (Fig. 1**i**) displayed that the characteristic peaks located at 855.1 and 872.7 eV belong to the Ni 2*p* 3/2 and Ni 2*p* 1/2 of Ni^{2+}, respectively. Notably, the binding energy of Ni 2*p* in P-$NiMoO_4$ shifted positively about 0.92 eV, which was attributed to the fact that P was more electronegative than Ni, resulting in a lower electron concentration around the center of Ni after P doping. For Mo 3*d* spectra, the two peaks of $NiMoO_4$ at 231.9 and 235.1 eV could be well indexed to Mo^{6+} (Fig. 1j) [31,32]. The peaks of Mo in Mo 3*d* XPS of P-$NiMoO_4$ could be deconvoluted into two components of Mo^{5+} and Mo^{6+} with the peaks of Mo $3d_{5/2}$ at 229.6 and 231.6 eV, respectively. The peaks of Mo^{5+} could be attributed to the reduction of a part of Mo^{6+} due to the doping of P atoms, the electron-rich Mo^{5+} had stronger nucleophilic properties, favoring the reduction reaction. In terms of O 1*s* (Figure S6c), the post-phosphating peaks significantly shifted towards higher binding energies [30]. The deconvoluted XPS spectrum demonstrated a dominant spectral component centered at 531.2 eV, corresponding to oxygen vacancy sites. This binding energy shift arises from the formation of PO_4^{3+} with more negative charges than MoO_4^{+} [33], which was balanced by the formation of O_v, supporting the formation of low-valence Mo (Mo^{5+}), and endowing the adsorption of xylose or water molecule in the electrocatalytic process.

3.2. *Performance in EXO*

The electrocatalytic properties of $NiMoO_4$/NF electrode were compared for EXO in 1.0 M KOH with and without 0.1 M xylose using the LSV in a three-electrode system (Figure S7). Remarkably, once xylose was added to the electrolyte, the overpotential was significantly reduced, which showed the more favorable catalytic reaction thermodynamics of EXO than OER (Figs. 2a and 2b). The EXO performance of $NiMoO_4$/NF electrode was then examined using different xylose concentrations (Figure S8). When the xylose concentration increased from 0.05 to 0.15 M, it was found that 0.1 M displayed the highest current density. However, when the xylose concentration increased from 0.1 to 0.15 M, the current density decreased, possibly due to the excessive xylose preventing the renewal of the active site on the catalyst surface. Fig. 2c further reflected the preference of EXO over OER of $NiMoO_4$/NF electrode. When the reaction system was operated at a constant potential, a sudden injection of xylose into the electrolyte resulted in a dramatic increase in the reaction current, indicating that $NiMoO_4$/NF electrode had a rapid and sensitive kinetic response to EXO. As shown in Fig. 2d, $NiMoO_4$/NF electrode showed the minimum overpotential and the steepest current response for EXO compared to NF and P-$NiMoO_4$/NF electrode at the same concentration of xylose. Notably, the overpotential of $NiMoO_4$/NF electrode was 130 mV lower than that of NF at 50 mA cm^{-2}, which strongly confirmed the high activity of $NiMoO_4$ catalyst against EXO. Intriguingly, the catalytic activity exceeded that of the commercial RuO_2 (Figure S9). Accordingly, the calculated Tafel slopes (Fig. 2e) of 32.0 mV·dec^{-1} for $NiMoO_4$/NF electrode was lower than that of NF (63.4 mV·dec^{-1}) and P-$NiMoO_4$/NF (38.3 mV·dec^{-1}) electrode, implying the better-advanced EXO kinetics [11,34]. This kinetic advantage was partly due to the strong adsorption capacity of xylose on $NiMoO_4$/NF electrode. To obtain the charge transfer capacity of the electrode-electrolyte interface, the prepared electrodes were then analyzed by EIS test (Fig. 2f and Figure S10). The charge transfer resistance (R_{ct}) of $NiMoO_4$/NF electrode was ~13.7 Ω during the EXO process, which was much smaller than that of NF (~30.8 Ω) and $NiMoO_4$/NF (~21.1 Ω) electrode, confirming the stronger charge transfer properties [35].

The ECSA was obtained using CV to probe the capacitance of the double layer (C_{dl}) in a 1.0 M KOH electrolyte within 0.1 M xylose (Fig. 2g and Figure S11). The C_{dl} value of $NiMoO_4$/NF electrode (188.5 mF cm^{-2}) was larger than that of the NF (53.1 mF cm^{-2}) and P-$NiMoO_4$/NF (131.5 mF cm^{-2}) electrode, which indicated that $NiMoO_4$/NF electrode has a much higher active surface area and more favorable surface adsorption kinetics for EXO. The original LSV current densities were normalized by ECSA (Figure S12), demonstrating that $NiMoO_4$/NF electrode maintained superior EXO activity compared to reference NF

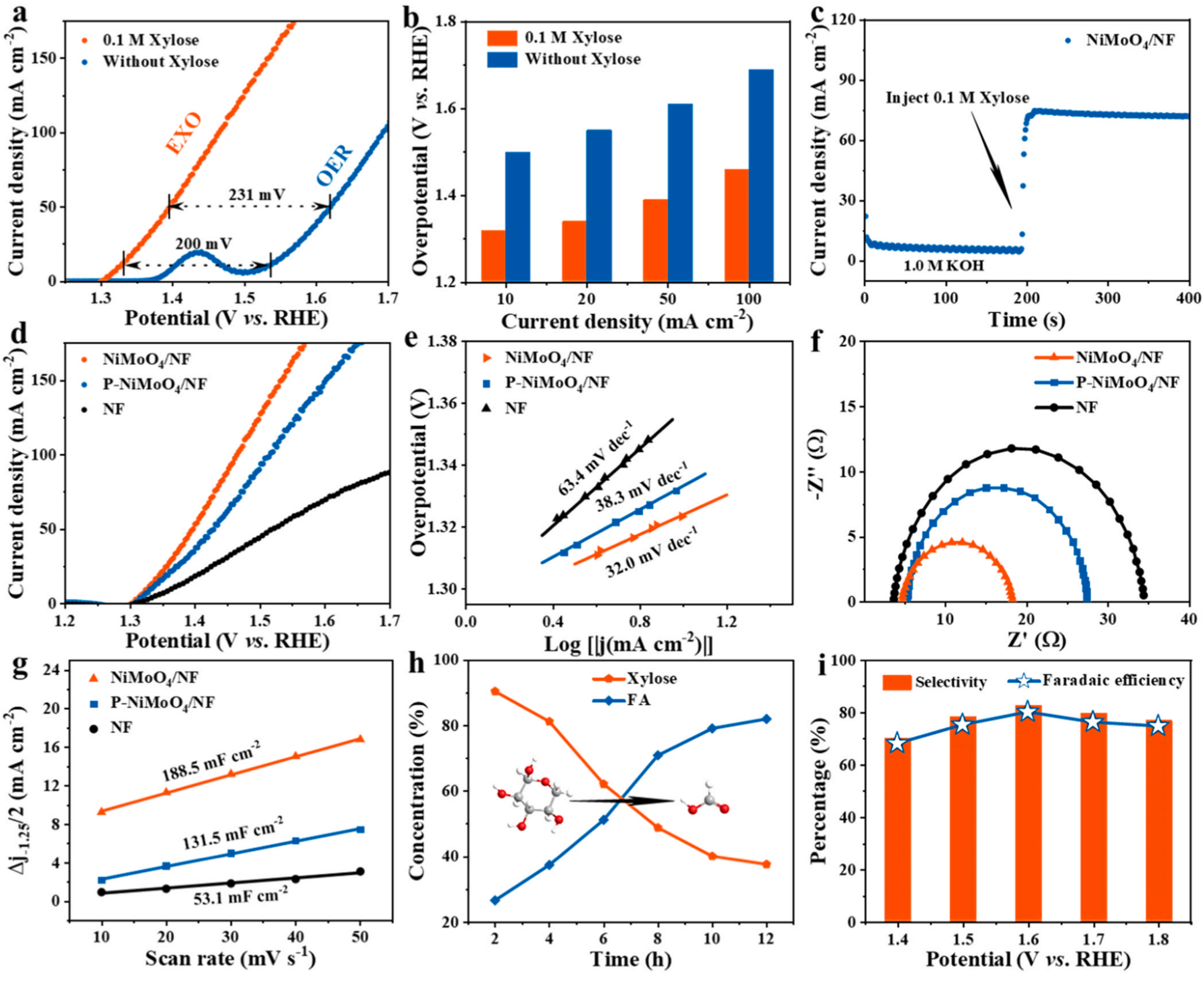

Fig. 2. Evaluation of the electrocatalytic EXO performance for $NiMoO_4$/NF electrode. (a) LSV curves of $NiMoO_4$/NF electrode in 1.0 M KOH without and with 0.1 M xylose, (b) Corresponding potentials at different current densities of $NiMoO_4$/NF electrode for EXO, (c) Chronoamperometry curve of $NiMoO_4$/NF electrode in 1.0 M KOH, (d) LSV curves, (e) Tafel slope, (f) Nyquist plots and (g) C_{dl} of $NiMoO_4$/NF, P-$NiMoO_4$/NF and NF electrodes in 1.0 M KOH with 0.1 M xylose, (h) The concentration curve of FA and xylose with time on $NiMoO_4$/NF electrode, (i) Selectivity and FE of FA on $NiMoO_4$/NF electrode at different potentials.

and P-NiMoO$_4$/NF electrode. The liquid products of EXO were analyzed by high performance liquid chromatography (HPLC). All reaction products were accurately quantified by the standard curve method (Figure S13 and S14). As shown in Fig. 2h, FA was slowly generated along with the consumption of xylose. The potential-dependent FA selectivity and FE showed a volcano trend and were best at 1.6 V$_{RHE}$ (Fig. 2i), reaching 82.7 % and 80.5 %, respectively. This is due to the fact that low potentials are not sufficient to drive the EXO, whereas too high potential leads to a more violent competition of HER. It is worth noting that, by combining the results of HPLC and nuclear magnetic resonance (NMR), it can be seen that in addition to the main product FA, the presence of by-products glyceraldehyde, lactic acid, and oxalic acid with low content was also detected (Figure S15). Combined with the above data and previous works [36,37], a possible reaction path for the electrooxidation of xylose to FA was reasonably speculated (Figure S16). Typically, xylose underwent isomerization to form its isomeride, which was subsequently converted to oxalic acid and glyceraldehyde via a retroaldol reaction, further oxidizing to FA. To verify the above-predicted reaction path, electrochemical tests were carried out with the possible intermediates as the starting substrate under the same reaction conditions. It can be seen from the obtained LSV curve (Figure S17) that the possible products exhibited a greater oxidation potential compared to xylose. Additionally, the results of product analysis (Table S2) indicated that EXO could finally obtain FA through the speculated pathway on the NiMoO$_4$/NF electrode. It is noted that under the action of the strong oxidizing OH* , the α-hydroxyl group of lactic acid can be oxidized to a ketone group, followed by the cleavage of the C-C bond and further oxidation decarboxylation to form oxalic acid, which can eventually also be converted into FA.

To further investigate the active species of NiMoO$_4$/NF electrode in the catalytic process of EXO, *operando* EPR experiment was performed using 5,5-dimethyl-1-pyrroline N-oxide (DMPO) as a trapping agent of hydroxyl radicals (Fig. 3a). The representative quadruple peaks of the DMPO-OH adduct were detected after holding the potential at 1.6 V$_{RHE}$ for 5 min, signifying the presence of active OH* intermediates [21]. Noticeably, the addition of xylose resulted in a significant enhancement of EPR signaling, confirming OH* as a surface-active substance that promoted EXO [38,39]. In addition, the presence of OH* promoting EXO was further verified by a rotating ring electrode (RRDE) test (Figs. 3b and 3c). There was no ring current when no disk current was applied. While the ring current was 5 μA at a disk current of 200 μA under 0.1 M xylose conditions (EXO), which was lower than the 30 μA under the absence of xylose, implying that the OER process was largely inhibited and more OH* was used to participated the kinetics EXO process, thus confirming the high FE toward EXO [40–42].

The Bode and Nyquist plots of OER and EXO driven by NiMoO$_4$/NF electrodes were obtained from *operando* EIS (Figure S18). In Bode plots, it was easy to notice that the EXO response peaks were shifted to a higher frequency compared to the OER response peaks (Figs. 3d and 3e), which may be caused by the interaction of OH* easily adsorbed to the NiMoO$_4$/NF electrode surface [35], consistent with the EPR and RRDE results. Furthermore, multi-potential step experiments were performed in three stages (Fig. 3f). First, active species of transition metal hydroxide were generated when a potential of 1.6 V$_{RHE}$ was applied. Then 0.1 M xylose was injected in the open-circuit potential state, and finally, the potential was set to 1.2 V$_{RHE}$ to analyze the potential chemical interactions between the metal actives and xylose. The findings indicated that the current response values remained virtually unchanged following the xylose addition. This suggested that both the activation of the metal-active substance and the oxidation of xylose were non-spontaneous. The production of OH* was concurrent with the oxidation of the active species, which further worked for the oxidation of xylose.

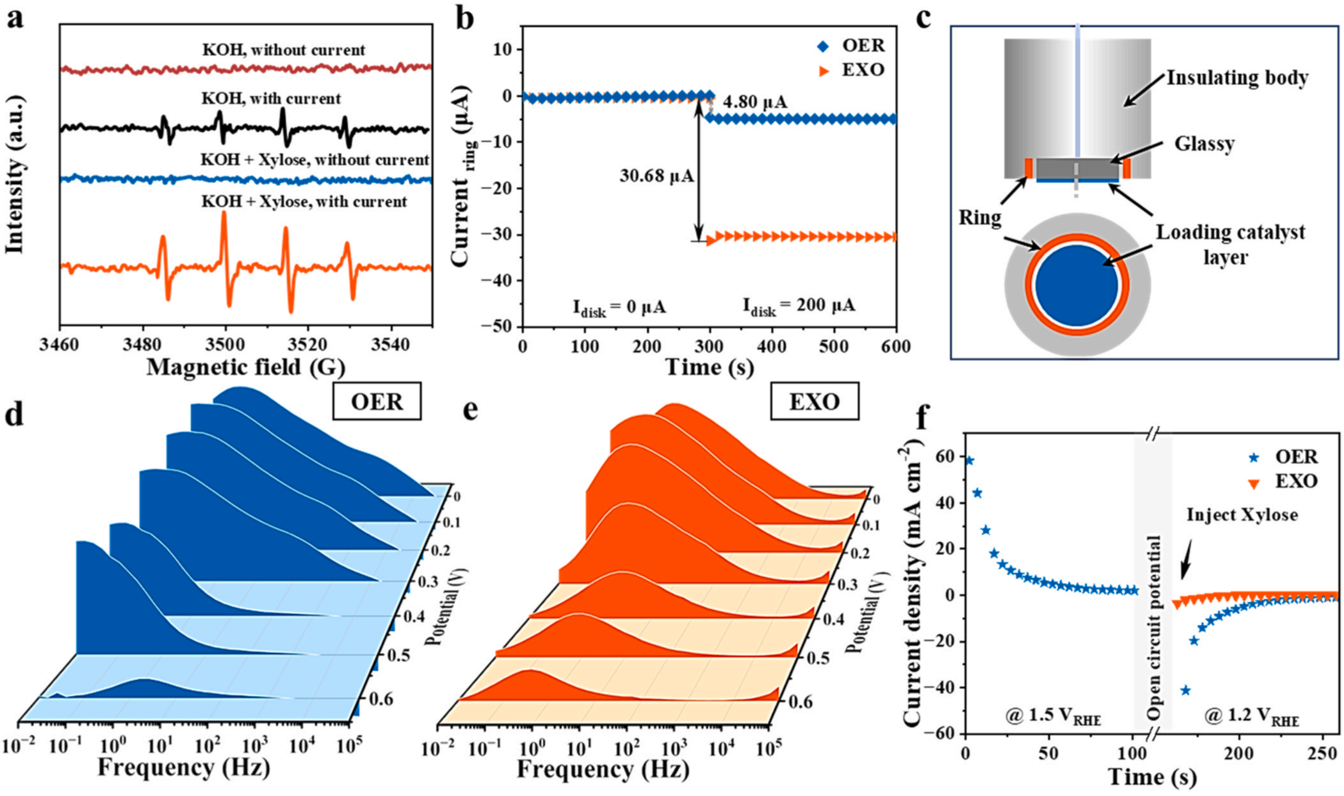

Fig. 3. Mechanism analysis. (a) *Operando* EPR trapping for hydroxyl radicals over NiMoO$_4$/NF electrode, (b) When the ring potential of OER and EXO is 0.4 V$_{RHE}$, the corresponding ring current on the RRDE, (c) Schematic diagram of RRDE device, *Operando* bode plots of (d) OER and (e) EXO, (f) Multi potential step experimental results.

3.3. Performance in HER

The activity of HER was further tested in the above three-electrode system. As displayed in Fig. 4a, the P-NiMoO$_4$/NF electrode demonstrated a lower overpotential, needing only 64 mV for 10 mA•cm^{-2} and 197 mV for 50 mA•cm^{-2}, which was lower than NF (298 and 517 mV) and NiMoO$_4$/NF (148 and 258 mV) electrode. This suggests that the HER activity of P-NiMoO/NF was improved by P doping, which was likely due to the fact that P doping adjusted the electronic structure (XPS demonstrated the appearance of Mo^{5+} after P doping), and the low valence species facilitated the formation of nucleophilic H, which affected the adsorption of HER intermediates (H*) [43,44]. This HER activity was also comparable to that of the state-of-the-art Pt/C and was only 3 mV higher at 10 mA cm^{-2}(Figure S19, Supporting Information). The corresponding Tafel slope of P-NiMoO$_4$/NF electrode (33.5 mV•dec^{-1}) was lower than that of NiMoO$_4$/NF electrode (39.9 mV•dec^{-1}) (Figs. 4b and 4c), which suggested that the P doping was conducive to speeding up HER kinetics [45], this may be related to the fact that the P-doped hierarchical microcolumn structure could expose more active sites and promote the desorption of bubbles. In short, the NiMoO$_4$/NF electrode possessed largely enhanced activity and reaction kinetics compared to the bare NF and NiMoO$_4$/NF electrode, as well as most of the reported HER catalysts (Fig. 4d and Table S3).

The interfacial charge transfer capacity of the as-prepared P-NiMoO$_4$/NF electrode was further analyzed by EIS. As shown in Fig. 4e, P-NiMoO$_4$/NF electrode had the lowest Rct, demonstrating its optimum charge transfer for HER [11,46,47]. This could be due to the strong electronic interaction that promoted electron transfer after P doping [31]. Furthermore, the ECSA was evaluated by the C$_{dl}$ value obtained at different scan rates of CV curves (Figure S20). The P-NiMoO$_4$/NF electrode exhibited a C$_{dl}$ value of 75.1 mF cm^{-2}, much larger than that of NF (43.2 mF cm^{-2}) and NiMoO$_4$/NF (52.6 mF cm^{-2}) electrode (Fig. 4f), implying that the unique hierarchical microcolumn array with porous structure together with P doping increased the effective active sites. The intrinsic activity of normalization by ECSA of P-NiMoO$_4$/NF electrode was also higher than the NF and NiMoO$_4$/NF electrode, further indicating the P doping improved HER performance of P-NiMoO$_4$/NF (Figure S21). Additionally, the intrinsic catalytic activities of different catalysts also could be evaluated by turnover frequency (TOF). By calculation, it was found that the P-NiMoO$_4$/NF electrode had higher TOF values (0.39 s^{-1} at an overpotential of 50 mV, and 0.93 s^{-1} at an overpotential of 100 mV) than that of the NiMoO$_4$/NF electrode

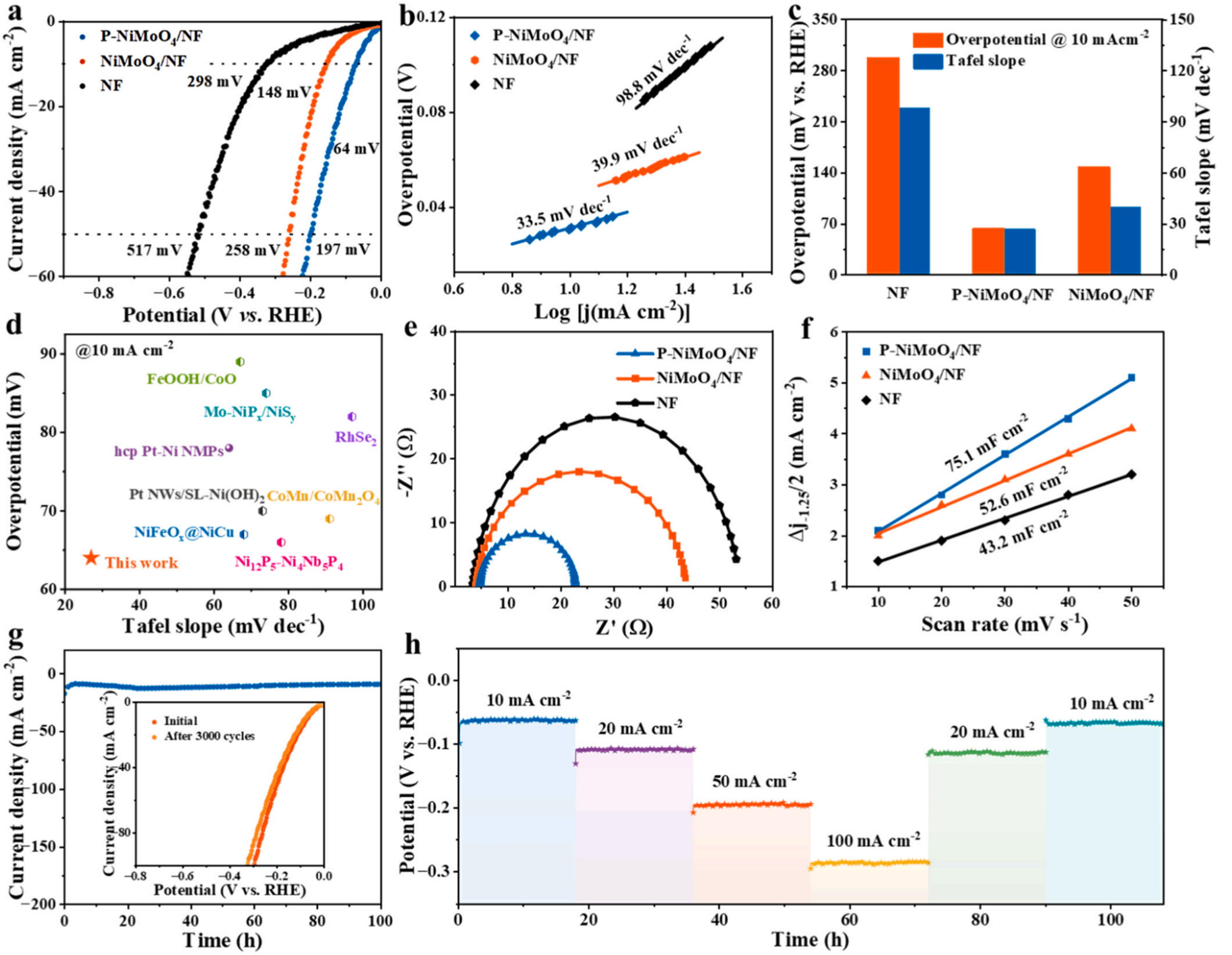

Fig. 4. HER electrochemical performance for P-NiMoO$_4$/NF electrode. (a) LSV curves and (b) Tafel slopes of P-NiMoO$_4$/NF, NiMoO$_4$/NF, and NF electrodes, (c) The Tafel slopes and the overpotentials at 10 mA cm^{-2} of P-NiMoO$_4$/NF, NiMoO$_4$/NF, and NF electrodes, (d) Comparison of P-NiMoO$_4$/NF electrode with reported advanced catalysts, (e) Nyquist plots and (f) C$_{dl}$ curves of P-NiMoO$_4$/NF, NiMoO$_4$/NF, and NF electrodes, (g) I-t curve of P-NiMoO$_4$/NF at 10 mA•cm^{-2} for HER durability, insert is the LSV curves before and after 3000 CV cycles, (h) Chronopotentiometry test of P-NiMoO$_4$/NF electrode for successive electrolysis at different current densities.

(0.09 s^{-1} at an overpotential of 50 mV, and 0.20 s^{-1} at an overpotential of 100 mV), indicating that the P-$NiMoO_4$/NF electrode indeed possessed higher intrinsic catalytic activity than the $NiMoO_4$/NF electrode (Figure S22). Promisingly, the electrocatalytic activity of P-$NiMoO_4$/NF electrode remained nearly unchanged after at least 100 h (Fig. 4g). The inset displayed that the polarization curve after 3000 cycles showed no significant decay compared to the initial HER activity, demonstrating its high durability. Moreover, chronopotentiometry tests revealed that the potentials remained nearly constant for up to 110 h at multiple consecutive current densities ranging from 10 to 100 mA cm^{-2} (Fig. 4h), further suggesting high durability.

3.4. Paired system

Inspired by the excellent performance displayed by $NiMoO_4$/NF and P-$NiMoO_4$/NF electrodes in EXO and HER, respectively, we paired these two discrete reactions to configure a coupled EXO||HER reaction system, aiming to concurrently achieve efficient xylose oxidation and H_2 production (Fig. 5a). LSV test results indicated a substantial enhancement in the synchronous reaction performance of the constructed EXO||HER system when compared to the conventional electrocatalytic water splitting, *i.e.*, the OER||HER system (Fig. 5b). At a cell voltage of 0.81 and 1.53 V, the EXO||HER system reached a current density of 10 and 50 mA cm^{-2}, respectively, which represented a significant reduction of 760 and 450 mV in the required input voltage compared to the OER||HER system (1.57 and1.98 V). This conclusively supported the feasibility of employing EXO in place of OER to facilitate highly efficient HER at the cathode [48]. The coupling performance also surpassed that of the most reported studies (Table S4). Concurrently, EXO application on the anode enabled the transformation of xylose into FA, a high-value chemical product. Within the EXO||HER system, prolonged constant-potential electrolysis reactions were conducted at a voltage of 1.6 V, with the anolyte being refreshed every 20 h as a run (Fig. 5c). It was observable that the trend of current density variation for each reaction run was essentially consistent, reflecting the high durability. Moreover, upon each renewal of the anolyte, a pronounced increase in the current level back to the initial value was noted. This phenomenon indicated that the decrease in current density was attributed to the significant reduction in xylose concentration, demonstrating the high efficiency of the catalyst in the oxidation of xylose.

Throughout five continuous runs, the conversion of xylose remained essentially stable, maintaining nearly 80 % (Fig. 5d). Concurrently, the FE of FA as a product consistently reached up to 80 %, demonstrating the high efficiency and stability of the $NiMoO_4$/NF electrode in the anodic EXO within the coupled system. Simultaneously, the H_2 produced by HER at the cathode was collected utilizing drainage (Figure S23). The results showed that the experimental yield of H_2 was in good agreement with the theoretical results (Fig. 5e). Moreover, FE was more than 93 % throughout the five runs (Fig. 5f). This fact likewise confirmed the high efficiency and durability of the P-$NiMoO_4$/NF electrode in the cathodic HER within the coupled system. SEM, XRD and XPS analyses demonstrated that the spent electrodes retained in nature with the preservation of their microcolumn feature and no obvious changes of chemical composition after EXO and HER tests (Figure S24, S25 and S26), further confirming its excellent robustness. Overall, the construction of a coupled reaction system leveraging the superior capabilities of $NiMoO_4$/NF and P-$NiMoO_4$/NF electrodes was of significant importance for the simultaneous oxidation of biomass and H_2 production.

4. Conclusions

In summary, we have successfully constructed the paired system efficient for electrocatalytic conversion of biomass monomer xylose into fine chemical FA and green H_2 production. The $NiMoO_4$/NF and P-$NiMoO_4$/NF electrodes with hierarchical microcolumn structures were successfully prepared through the hydrothermal tandem and then annealing methods. The as-prepared $NiMoO_4$/NF electrode exhibited excellent EXO performance in the alkaline electrolyte, with 200 and 230 mV reduction of the overpotential at 10 and 50 mA cm^{-2},

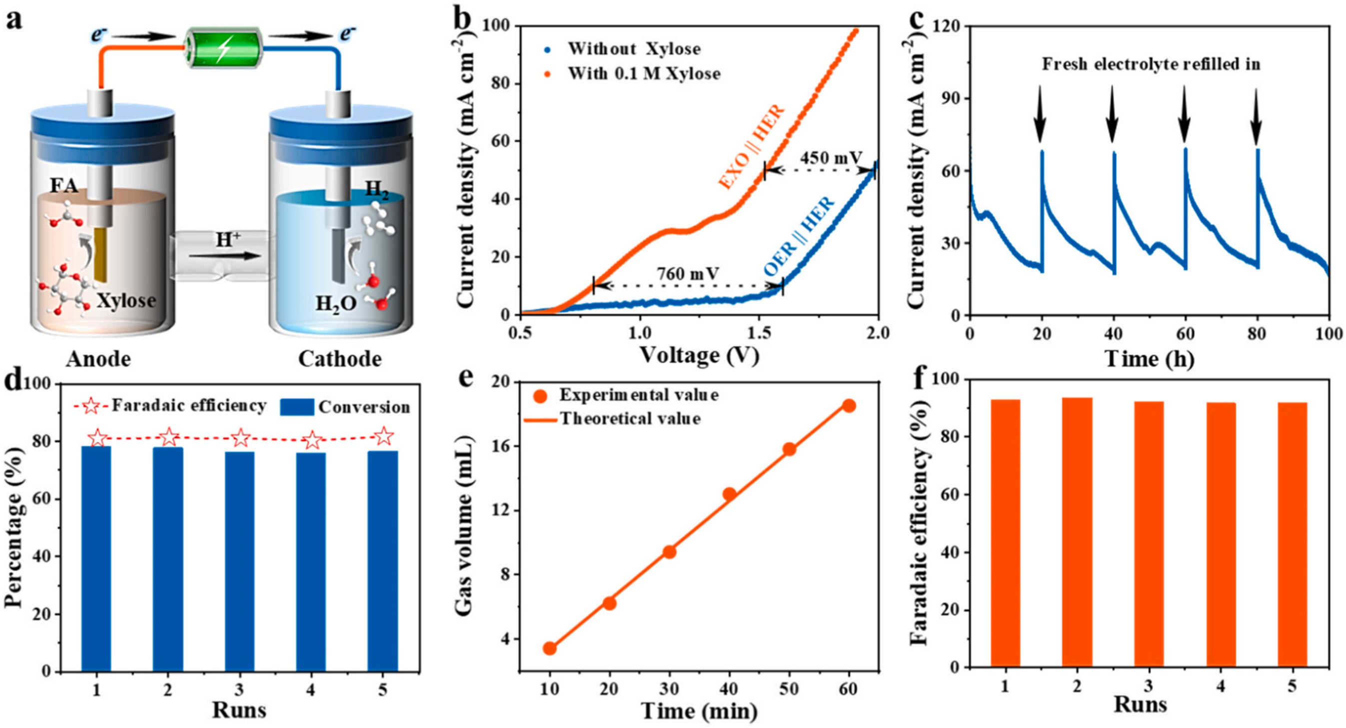

Fig. 5. (a) Schematic illustration of $NiMoO_4$/NF || P-$NiMoO_4$/NF electrolyzer for both EXO and HER, (b) Polarization curves of EWS and xylose electrolysis, (c) Chronoamperometry curve of durability test of 5 runs for EXO, (d) Xylose conversion rate and FE of each run, (e) Comparison in the actual and theoretical H_2 production rate, (f) H_2 production FE of each run.

respectively, compared to the OER. While the P-$NiMoO_4$/NF electrode manifested a gratifying electrocatalytic activity and durability for alkaline HER with a low overpotential of 64 and 197 mV for 10 and 50 mA•cm^{-2}, respectively, and maintaining high durability over 110 h across various current densities. These are far superior to most previously reported catalysts. The mechanism studies confirmed that OH* and H* intermediates are effective active species in promoting EXO and HER, respectively. By pairing the EXO with HER, the full cell voltage to reach 10 and 50 mA cm^{-2} dramatically reduces to 0.81 and 1.53 V, respectively, for the sustainable synthesis of valuable FA and green H_2 maintaining over 100 h. The coupling performance surpassed that of the most previously reported studies. This study provides a promising strategy for biomass refining and green H_2 generation.

CRediT authorship contribution statement

Bin Liu: Conceptualization, Investigation, Formal analysis, Writing – original draft. **Huiming Wen:** Resources, Writing – review & editing, Supervision. **Xiaoying Liang:** Investigation, Formal analysis, Writing – original draft. **Bo Da:** Conceptualization, Validation. **Ke Li:** Validation, Software. **Zhenhao Xu and Xiaodie Zhang:** Formal analysis, Writing – review & editing. **Yutong Zhang:** Validation, Formal analysis, Visualization. **Yuchen Wang:** Conceptualization, Supervision. **Hao Li:** Conceptualization, Supervision, Project administration, Writing – review & editing. **Kai Yan:** Conceptualization, Validation, Project administration, Supervision, Writing – review & editing.

Declaration of Competing Interest

The authors declare that they have no known competing financial interests or personal relationships that could have appeared to influence the work reported in this paper.

Acknowledgments

This work was supported by the National Key Research and Development Program of China (No. 2024YFE0203000), the National Natural Science Foundation of China (22078374, 22378434), and the Scientific and Technological Planning Project of Guangzhou (No. 2024A04J4353).

Appendix A. Supporting information

Supplementary data associated with this article can be found in the online version at doi:10.1016/j.apcatb.2025.125443.

Data Availability

Data will be made available on request.

References

[1] C. Panda, P.W. Menezes, S. Yao, J. Schmidt, C. Walter, J.N. Hausmann, M. Driess, Boosting electrocatalytic hydrogen evolution activity with a $NiPt_3$@NiS heteronanostructure evolved from a molecular Nickel–Platinum precursor, J. Am. Chem. Soc. 141 (2019) 13306–13310.

[2] H. Ren, M. Kovalev, Z. Weng, M.Z. Muhamad, H. Ma, Y. Sheng, L. Sun, J. Wang, S. Rihm, W. Yang, A.A. Lapkin, J.W. Ager, Operando proton-transfer-reaction time-of-flight mass spectrometry of carbon dioxide reduction electrocatalysis, Nat. Catal. 5 (2022) 1169–1179.

[3] R. Guo, Y. Zeng, L. Lin, D. Hu, C. Lu, S. Conroy, S. Zhang, C. Zeng, H. Luo, Z. Jiang, X. Zhang, X. Tu, K. Yan, CO_2-assisted controllable synthesis of PdNi nanoalloys for highly selective hydrogenation of biomass-derived 5-hydroxymethylfurfural, Angew. Chem. Int. Ed. (2024) e202418234.

[4] S. Aslam, S. Rani, K. Lal, M. Fatima, T. Hardwick, B. Shirinfar, N. Ahmed, Electrochemical hydrogen production: sustainable hydrogen economy, Green. Chem. 25 (2023) 9543–9573.

[5] K. Veeramani, G. Janani, J. Kim, S. Surendran, J. Lim, S.C. Jesudass, S. Mahadik, H. lee, T.H. Kim, J.K. Kim, U. Sim, Hydrogen and value-added products yield from hybrid water electrolysis: a critical review on recent developments, Renew. Sust. Energ. Rev. 177 (2023) 113227.

[6] Z.H. Pan, Z.Z. Weng, X.J. Kong, L.S. Long, L.S. Zheng, Lanthanide-containing clusters for catalytic water splitting and CO_2 conversion, Coord. Chem. Rev. 457 (2022) 214419.

[7] M. Zhang, Z. Zheng, X. Zhang, Z. Jiang, X. Yong, K. Li, X. Tu, K. Yan, Pairing electrocatalytic reduction and oxidation of biomass-derived 5-hydroxymethylfurfural into highly value-added chemicals, JACS Au 5 (2025) 937–947.

[8] T. Capurso, M. Stefanizzi, M. Torresi, S.M. Camporeale, Perspective of the role of hydrogen in the 21st century energy transition, Energy Convers. Manag. 251 (2022) 114898.

[9] H. Luo, P. Yu, G. Li, K. Yan, Topological quantum materials for energy conversion and storage, Nat. Rev. Phys. 4 (2022) 611–624.

[10] Z. Zheng, B. Liu, J. Qiu, S. Xu, Y. Wang, M. Zhang, K. Li, Z. Sun, Z. Li, Y. Wan, C.R. A. Catlow, K. Yan, Effectively regulating electrooxidation of formic acid over bimetallic PtCo alloys via the integration of theory and experiment, ACS Catal. 14 (2024) 18333–18344.

[11] Y. Li, Y. Jiao, H. Yan, G. Yang, Y. Liu, C. Tian, A. Wu, H. Fu, Mo-Ni-based heterojunction with fine-customized d-band centers for hydrogen production coupled with benzylamine electrooxidation in low alkaline medium, Angew. Chem. Int. Ed. 62 (2023) e202306640.

[12] Y. Lum, J.E. Huang, Z. Wang, M. Luo, D.H. Nam, W.R. Leow, B. Chen, J. Wicks, Y. C. Li, Y. Wang, C.T. Dinh, J. Li, T.T. Zhuang, F. Li, T.K. Sham, D. Sinton, E. H. Sargent, Tuning OH binding energy enables selective electrochemical oxidation of ethylene to ethylene glycol, Nat. Catal. 3 (2020) 14–22.

[13] R.A. Senthil, S. Jung, A. Min, A. Kumar, C.J. Moon, M. Singh, M.Y. Choi, Revealing the impact of pulsed laser-produced single-Pd nanoparticles on a bimetallic $NiCo_2O_4$ electrocatalyst for energy-saving hydrogen production via hybrid water electrolysis, ACS Catal. 14 (2024) 3320–3335.

[14] Y. Liu, J. Zhang, Y. Li, Q. Qian, Z. Li, Y. Zhu, G. Zhang, Manipulating dehydrogenation kinetics through dual-doping Co_3N electrode enables highly efficient hydrazine oxidation assisting self-powered H_2 production, Nat. Commun. 11 (2020) 1853.

[15] Q. Qian, J. Zhang, J. Li, Y. Li, X. Jin, Y. Zhu, Y. Liu, Z. Li, A. El-Harairy, C. Xiao, G. Zhang, Y. Xie, Artificial heterointerfaces achieve delicate reaction kinetics towards hydrogen evolution and hydrazine oxidation catalysis, Angew. Chem. Int. Ed. 60 (2021) 5984–5993.

[16] K. Shi, D. Si, X. Teng, L. Chen, J. Shi, Pd/$NiMoO_4$/NF electrocatalysts for the efficient and ultra-stable synthesis and electrolyte-assisted extraction of glycolate, Nat. Commun. 15 (2024) 2899.

[17] F.M. Li, C. Xia, W. Fang, Y. Chen, B.Y. Xia, RhCuBi trimetallenes with composition segregation coupled crystalline-amorphous heterostructure toward ethanol electrooxidation, Adv. Energy Mater. (2024) 2400112.

[18] D. Li, X. Zhou, Q. Ruan, L. Liu, J. Liu, B. Wang, Y. Wang, X. Zhang, R. Chen, H. Ni, C. Huang, H. Wang, P.K. Chu, Suppression of passivation on nickel hydroxide in electrocatalytic urea oxidization, Adv. Funct. Mater. 34 (2023) 2313680.

[19] H.A. Bandal, H. Kim, In situ construction of Fe_3O_4@FeOOH for efficient electrocatalytic urea oxidation, J. Colloid Interface Sci. 627 (2022) 1030–1038.

[20] F.O. Boakye, M.G. Sendeku, A. Kumar, S. Ajmal, K.A. Owusu, K.B. Ibrahim, M. Tabish, Fu Zaman, M.A. Mushtaq, K.M. Alotaibi, M.Z. Ansari, G. Yasin, Engineering active sites on binary metal selenide heterointerface catalyst to boost urea electrooxidation, Appl. Catal. B Environ. 352 (2024) 124013.

[21] W. Tang, L. Zhang, T. Qiu, H. Tan, Y. Wang, W. Liu, Y. Li, Efficient conversion of biomass to formic acid coupled with low energy consumption hydrogen production from water electrolysis, Angew. Chem. Int. Ed. 62 (2023) e202305843.

[22] H. Wang, Q. Wang, Y. Wu, J. Peng, X.-K. Gu, M. Ding, Dualoriented selectivity switching for highly efficient biomass upgrading via selective C–O bond activation, ACS Catal. 12 (2022) 12027–12035.

[23] X. Wu, Z. Zhao, X. Shi, L. Kang, P. Das, S. Wang, S. Chu, H. Wang, K. Davey, B. Zhang, S. Qiao, J. Gong, Z. Wu, Multi-site catalysis of high-entropy hydroxides for sustainable electrooxidation of glucose to glucaric acid, Energy Environ. Sci. 17 (2024) 3042–3051.

[24] J. Choi, S. Seo, M. Kim, Y. Han, X. Shao, H. Lee, Relationship between structure and performance of atomic-scale electrocatalysts for water splitting, Small (2023) 2304560.

[25] Y.J. Son, S. Kim, V. Leung, K. Kawashima, J. Noh, K. Kim, R.A. Marquez, O. A. Carrasco-Jaim, L.A. Smith, H. Celio, D.J. Milliron, B.A. Korgel, C.B. Mullins, Effects of electrochemical conditioning on nickel-based oxygen evolution electrocatalysts, ACS Catal. 12 (2022) 10384–10399.

[26] Y. An, X. Long, M. Ma, J. Hu, H. Lin, D. Zhou, Z. Xing, B. Huang, S. Yang, One-step controllable synthesis of catalytic Ni_4Mo/MoO_x/Cu nanointerfaces for highly efficient water reduction, Adv. Energy Mater. 9 (2019) 1901454.

[27] Z. Zhao, J. Sun, Z. Li, X. Xu, Z. Zhang, C. Li, L. Wang, X. Meng, Rapid synthesis of efficient Mo-based electrocatalyst for the hydrogen evolution reaction in alkaline seawater with 11.28% solar-to-hydrogen efficiency, J. Mater. Chem. A 11 (2023) 10346–10359.

[28] K. Wang, H. Du, S. He, L. Liu, K. Yang, J. Sun, Y. Liu, Z. Du, L. Xie, W. Ai, W. Huang, Kinetically controlled, scalable synthesis of γ-FeOOH nanosheet arrays on nickel foam toward efficient oxygen evolution: The key role of in-situ-generated γ-NiOOH, Adv. Mater. 33 (2021) 2005587.

[29] H. Kim, K. Min, G. Song, J. Kim, H.C. Ham, S.-H. Baeck, Hollow-structured cobalt sulfide electrocatalyst for alkaline oxygen evolution reaction: Rational tuning of electronic structure using iron and fluorine dual-doping strategy, J. Colloid Interface Sci. 665 (2024) 922–933.

[30] Z. Yu, C. Lang, M. Gao, Y. Chen, Q. Fu, Y. Duan, S. Yu, Ni–Mo–O nanorod-derived composite catalysts for efficient alkaline water-to-hydrogen conversion via urea electrolysis, Energy Environ. Sci. 11 (2018) 1890–1897.

[31] Z. Zhao, Z. Li, Z. Zhang, X. Meng, Fe/P dual-doping $NiMoO_4$ with hollow structure for efficient hydrazine oxidation-assisted hydrogen generation in alkaline seawater, Appl. Catal. B Environ. 347 (2024) 123805.

[32] G. Solomon, A. Landström, R. Mazzaro, M. Jugovac, P. Moras, E. Cattaruzza, V. Morandi, I. Concina, A. Vomiero, $NiMoO_4$@Co_3O_4 core–shell nanorods: In situ catalyst reconstruction toward high efficiency oxygen evolution reaction, Adv. Energy Mater. 11 (2021) 2101324.

[33] G. Li, H. Jang, S. Liu, Z. Li, M.G. Kim, Q. Qin, X. Liu, J. Cho, The synergistic effect of Hf-O-Ru bonds and oxygen vacancies in Ru/HfO_2 for enhanced hydrogen evolution, Nat. Commun. 13 (2022) 1270.

[34] G. Yang, Y. Jiao, H. Yan, Y. Xie, C. Tian, A. Wu, Y. Wang, H. Fu, Unraveling the mechanism for paired electrocatalysis of organics with water as a feedstock, Nat. Commun. 13 (2022) 3125.

[35] Y. Duan, M. Xue, B. Liu, M. Zhang, Y. Wang, B. Wang, R. Zhang, K. Yan, Integration of theory prediction and experimental electrooxidation of glycerol on $NiCo_2O_4$ nanosheets, Chin. J. Catal. 57 (2024) 68–79.

[36] S. Kiatphuengporn, A. Junkaew, C. Luadthong, S. Thongratkaew, C. Yimsukanan, S. Songtawee, T. Butburee, P. Khemthong, S. Namuangruk, M. Kunaseth, K. Faungnawakij, Roles of acidic sites in alumina catalysts for efficient d-xylose conversion to lactic acid, Green. Chem. 22 (2020) 8572–8583.

[37] L.S. M. S, K.M. Nampoothiri, Xylose dehydrogenase immobilized on ferromagnetic nanoparticles for bioconversion of xylose to xylonic acid, Bioconjugate Chem. 33 (2022) 948–955.

[38] B. Liu, Z. Zheng, Y. Liu, M. Zhang, Y. Wang, Y. Wan, K. Yan, Efficient electrooxidation of biomass-derived aldehydes over ultrathin NiV-layered double hydroxides films, J. Energy Chem. 78 (2023) 412–421.

[39] L. Gouda, L. Sévery, T. Moehl, E. Mas-Marzá, P. Adams, F. Fabregat-Santiago, S. D. Tilley, Tuning the selectivity of biomass oxidation over oxygen evolution on NiO-OH electrodes, Green. Chem. 23 (2021) 8061–8068.

[40] R. Fan, X. Zhai, W. Qiao, Y. Zhang, N. Yu, N. Xu, Q. Lv, Y. Chai, B. Dong, Optimized electronic modification of S-doped CuO induced by oxidative reconstruction for coupling glycerol electrooxidation with hydrogen evolution, Nano-Micro Lett. 15 (2023) 190.

[41] R.N. Dürr, P. Maltoni, H. Tian, B. Jousselme, L. Hammarström, T. Edvinsson, From $NiMoO_4$ to γ-NiOOH: Detecting the active catalyst phase by time resolved in situ and operando raman spectroscopy, ACS Nano 15 (2021) 13504–13515.

[42] I. Mondal, J.N. Hausmann, G. Vijaykumar, S. Mebs, H. Dau, M. Driess, P. W. Menezes, Nanostructured intermetallic nickel silicide (pre)catalyst for anodic oxygen evolution reaction and selective dehydrogenation of primary amines, Adv. Energy Mater. 12 (2022) 2200269.

[43] Z. Xu, J. Zhu, Z. Shu, Y. Xia, R. Chen, S. Chen, Y. Wang, L. Zeng, J. Wang, Y. Cai, S. Chen, F. Huang, H.-L. Wang, Phosphorus-induced anti-growth of ruthenium clusters-single atoms for ultra-stable hydrogen evolution over 100,000 cycles, Joule 8 (2024) 1–14.

[44] F.-C. Pan, J. Jia, F. Gong, Y. Liu, S. Liu, S.C. Jun, D. Lin, Y. Guo, Y. Yamauchi, Y. Huo, Heterometallic electrocatalysts derived from high-nuclearity metal clusters for efficient overall water splitting, ACS Nano 18 (2024) 6202–6214.

[45] H.-G. Gim, E. Park, J. Ha, J. Lee, Y.-T. Kim, J. Choi, Bifunctional phosphorus-doped NiMo oxide/Ni–Fe hydroxide composite for overall water electrolysis: optimized performance with exceptional stability, Mater. Today Energy 41 (2024) 101526.

[46] T.G. Vo, G.S. Tran, C.L. Chiang, Y.G. Lin, H.E. Chang, H.H. Kuo, C.Y. Chiang, Y. J. Hsu, Au@NiS_x yolk@shell nanostructures as dual-functional electrocatalysts for concomitant production of value-added tartronic acid and hydrogen fuel, Adv. Funct. Mater. 33 (2022) 2209386.

[47] Z. Zhang, L. Li, Y. Li, Y. Zheng, Q. Wu, L. Xie, B. Luo, J. Hao, W. Shi, Activating MoO_4 tetrahedrons to MoO species in MoNi alloy for boosting performance in alkaline hydrogen evolution reaction, Chem. Eng. J. 469 (2023) 143846.

[48] C. Chen, Z. Fu, F. Qi, Y. Chen, G. Meng, Z. Chang, F. Kong, L. Zhu, H. Tian, H. Huang, X. Cui, J. Shi, Fe^{2+}/Fe^{3+} cycling for coupling self-powered hydrogen evolution and preparation of electrode catalysts, Angew. Chem. Int. Ed. 61 (2022) e202207226.